Article

Enhanced Activity and Stability of Carbon-Decorated Cuprous Oxide Mesoporous Nanorods for CO2 Reduction in Artificial Photosynthesis

Luo Yu, Guojian Li, Xiaoshu Zhang, Xin Ba, Guodong Shi, Yong Li, Po Keung Wong, Jimmy Chai Mei Yu, and Ying Yu

ACS Catal., **Just Accepted Manuscript** • DOI: 10.1021/acscatal.6b01455 • Publication Date (Web): 22 Aug 2016

Enhanced Activity and Stability of Carbon-Decorated Cuprous Oxide Mesoporous Nanorods for CO_2 Reduction in Artificial Photosynthesis

Luo Yu[a], Guojian Li[a], Xiaoshu Zhang[a], Xin Ba[a], Guodong Shi[a], Yong Li[a], Po Keung Wong[b], Jimmy C. Yu[c] and Ying Yu[a]*

[a] College of Physical Science and Technology, Central China Normal University, Wuhan 430079, China

[b] School of Life Science, The Chinese University of Hong Kong, Shatin, NT, Hong Kong SAR, China

[c] Department of Chemistry, The Chinese University of Hong Kong, Shatin, NT, Hong Kong SAR, China

* Corresponding author. Tel: 86-27-67867037; email: yuying01@mail.ccnu.edu.cn

ABSTRACT:

The development of photocatalysts with superior activity and stability to produce organic fuels through CO_2 reduction under renewable sunlight is of great significance due to the depletion of fossil fuels and severe environmental problems. In this study, we presented a "hitting three birds with one stone" strategy to synthesize carbon layer coated cuprous oxide (Cu_2O) mesoporous nanorods on Cu foils via a facile chemical oxidation and subsequent carbonization method. The thin carbon layer not only works as a protective layer to quench the common photocorrosion problem of Cu_2O, but also endows the sample a mesoporous and one-dimensional nanorod structure, which can facilitate reactant molecule adsorption and charge carrier transfer. Substantially, the coated samples exhibited remarkably improved stability as well as decent activity for CO_2 reduction under visible light irradiation. The optimized sample attained an apparent quantum efficiency of 2.07% for CH_4 and C_2H_4 at λ_0 = 400 nm, and 93% activity remained after six photoreduction cycles under visible light. This work provides a facile strategy to address the stability and activity issues of Cu_2O under visible light irradiation, which is presumably suitable for other semiconductors as promising candidates for CO_2 reduction in artificial photosynthesis.

KEYWORDS: Cu_2O mesoporous nanorods, carbon coating, photocatalysis, CO_2 reduction, stability, visible light

1. INTRODUCTION

The deepening crisis of greenhouse effect and depletion of fossil resources are becoming enormous threats to sustainable development. To convert CO_2 into fuel is considered to be a win-win strategy since it has the potential not only to generate valuable fuels but also to mitigate the negative effect of anthropogenic CO_2 over-emission.[1-3] Noticeably, artificial photosynthesis has been regarded as a promising way to achieve CO_2 reduction for fuel production by using solar energy.[4] Beyond doubt, photocatalysts play vital roles in the conversion process so that developing such materials with good activity and stability is of great significance.

Since the pioneering work of photoreduction of CO_2 to organic compounds by Inoue et al.,[5] as one of the earliest studied photocatalysts, titanium dioxide (TiO_2) has been proverbially investigated due to its low-cost, nontoxicity and high stability.[6,7] Notwithstanding, the narrow scope of light absorption (< 387 nm) and high light-induced electron-hole recombination rate restrict its photocatalytic performance.[8] Therefore, extensive research efforts have been made to explore other suitable semiconductor materials as efficient photocatalysts for CO_2 conversion. To date, multifarious materials including metal complexes,[9,10] organic compounds,[11] metal oxide,[12-14] metal sulfides,[15] graphitic compounds,[16] and their composites[17-20] have been reported. Among these materials, cuprous oxide (Cu_2O) is considered to be one of the most promising candidates for solar energy conversion. It is known that Cu_2O is a semiconductor with direct band gap of about 2.0 eV, which guarantees efficient visible light absorption.[21] Moreover, Cu_2O possesses favorable energy band

positions with the conduction band lying up CO_2 reduction potential, which facilitates the reduction of CO_2 to hydrocarbon fuels.[22] Additionally, Cu_2O is abundant, low-cost and environmentally friendly.[23]

It is generally acknowledged that the photocatalytic reduction of CO_2 mainly involves charge carrier generation, charge carrier transfer, and finally, multielectron chemical reduction on particular active sites.[4] Since Cu_2O is responsive to visible light, the first step of the charge carrier generation is efficiently achievable under visible light. Whereas, on account of poor conductivity, the process of charge carrier transfer is severely confined for this photocatalyst, and vast electron-hole pairs recombine during their migration to the surface.[24] The last step of reduction on active sites is not only compromised by the recombination of electron-hole pairs, but also related to the structure of Cu_2O. Besides, the photocorrosion problem is an inherent drawback for Cu_2O-based photocatalysts, in which the cuprous ion (Cu^+) is highly prone to be oxidized to cupric ion (Cu^{2+}) or reduced to copper (Cu).[25] The unstable character for Cu_2O hampers its practical application severely.

To ameliorate the performance of Cu_2O in photocatalytic reactions, the strategies including doping,[26] structure engineering,[27] exposed facet engineering,[28] and semiconductor compositing[29] etc. have been employed. Substantially, one-dimensional (1-D) nanostructures, including nanowire, nanorod and nanotube, are highly attractive building blocks owing to their inherent anisotropies and electron efficient transport within the smallest dimension.[30,31] Cu_2O nanowires has been reported to have the enhanced activity for water splitting.[32] In addition, protective

layer coating is also one of the most effective and handy solutions to improve stability as well as conductivity for Cu_2O. As a promising material widely applied in energy conversion field, carbon is so appropriate to serve as a coating layer for its unique physicochemical properties, such as strong mechanical strength, nontoxicity, excellent electronic and thermal conductivity, and solution processing feasibility.[33] Recently, it was reported that a sandwich-like structure with NiFe nanoparticles encapsulated in coupled graphene sheets (NiFe/C) showed oxygen evolution with high efficiency,[34] since the coupled graphene sheets around active catalysts accelerated electron transfer and prevented NiFe nanoparticles from aggregation during long-time electrochemical reactions. Additionally, CdS petalous nanostructures coated with a thin carbon layer displayed remarkably improved photostability and activity due to that the carbon layer not only significantly reduced the amount of surface traps, but also provided perfect chemical protection for inner CdS nanoparticles.[35] Furthermore, porous structure is extraordinarily beneficial in a photocatalytic process for it can provide large specific area and many active sites, which facilitates reactant molecule adsorption and reaction.[24] In particular, improving the CO_2 adsorption ability of photocatalysts has been regarded as an efficient approach to enhance CO_2 conversion efficiency. To the best of our knowledge, so far, there has been no report about the combination of 1-D nanostructure, carbon coating and mesoporous structure for Cu_2O as a photocatalyst for artificial photosynthesis.

Herein, we presented a facile and economical approach to synthesize carbon layer coated cuprous oxide mesoporous nanorods (CCMNRs) for CO_2 reduction under

visible light. Firstly, $Cu(OH)_2$ nanotubes (NTs) were synthesized directly on a Cu foil through a handy method of chemical oxidation. Subsequently, the obtained $Cu(OH)_2$ NTs were dipped into glucose solution, which was used as a green carbon source. Then the glucose coated $Cu(OH)_2$ NTs were calcined in N_2 atmosphere to obtain CCMNRs. This facial "hitting three birds with one stone" strategy endowed the samples with three characteristics: coating protective carbon layer, mesoporous structure and 1-D nanorod structure, all of which brought about the favorably robust performance and superior stability for as-prepared CCMNRs as the photocatalysts used for CO_2 reduction under visible light.

2. EXPERIMENTAL SECTION

2.1. Materials synthesis. All of the chemicals used in this study and copper foil with purity of 99.98% were purchased from Shanghai Guoyao Chemicals Ltd. Co. The chemicals were analytical reagents and used without further purification. Deionized water was used for the preparation of all aqueous solutions. In this study, $Cu(OH)_2$ NTs was synthesized through a modified chemical oxidation method,[36] and a typical process was as follows. A piece of Cu foil with a size of 2×5 cm^2 and a thickness of 0.2 mm was cleaned in hydrochloric acid (37%) and then ultrasonically in acetone and ethanol for 5 min sequentially. The cleaned Cu foil was then immersed into 80 mL aqueous solution containing 2.5 M NaOH and 0.125 M $(NH_4)_2S_2O_8$ for 20 min. Notably, a temperature of about 3℃ remained for the solution during the reaction to prevent $Cu(OH)_2$ NTs from agglomeration. Finally, the Cu foil with a light

blue color was taken out from the solution, rinsed with deionized water, and dried in air. Afterward, the prepared $Cu(OH)_2$ NTs had immerged into an aqueous glucose solution for about 12 h. Then, they were dried at ambient condition, and annealed at 500℃ in N_2 atmosphere for 2 h to form CCMNRs. The concentration of the glucose solution was varied to control the carbon layer thickness of the CCMNRs. For comparison, without glucose, the as-prepared $Cu(OH)_2$ NTs was directly annealed at 500℃ in N_2 atmosphere for 2 h, which was labeled with Cu_2O.

2.2. Materials characterization. The morphology of the prepared samples was detected with scanning electron microscopy (SEM) with the model of JEOL JSM-6700, transmission electron microscopy (TEM) and dark-field scanning transmission electron microscopy (DF-STEM) with the model of JEOL JEM-2100F coupled with an energy dispersive X-ray spectroscopy (EDS), operated with an accelerating voltage of 200 kV. X-ray powder diffraction (XRD) patterns of the samples were analyzed by using a PANalytical diffractometer (D/max 40kv) using Cu Kα radiation (λ=0.154598 nm) for crystalline phase. The surface X-ray diffraction (SXRD) measurements for thin film sample were performed in theta/theta mode with a step width of 0.02° and a scan rate 100 s/step. The surface chemical analysis of the samples was achieved with X-ray Photoelectron Spectroscopy (XPS) (VG Multiab-2000) using a PHI Quantum 2000 XPS system with a monochromatic Al Kα source and charge neutralizer. All of the spectra were calibrated to C1s peak at 284.6 eV. The UV-vis diffuse reflectance spectra (UV-vis DRS) were recorded with PerkinElmer Lambda 35 Spectrophotometer in the range of 400-800 nm using $BaSO_4$

as a reference. Raman spectra were collected at room temperature using a LabRAMHR Raman system under Ar^+ (532 nm) laser excitation. Micromeritics ASAP2020 nitrogen adsorption apparatus (USA) was used to characterize the Brunauer-Emmett-Teller (BET) specific surface area of the samples. CO_2 adsorption isotherms were measured at room temperature using a BEL SORP-mini II (BEL Japan). Pulsed CO chemisorption capacity for the different samples was tested using a BELCAT-B-293 Catalyst Analyzer (BEL Japan), equipped with a thermal conductivity detector (TCD) to measure CO consumption. Generally, each sample (63.6 mg) was placed in a U-type quartz tube and pretreated at 573 K with a helium flow (50 cm^3 min^{-1}) for 20 min and then maintained in the helium atmosphere at the same temperature for 15 min. After pretreatment, the sample was cooled down to 323 K and maintained at the temperature for 10 min. Then CO (CO/He, 10%) pulses were injected from a constant volume loop valve into the U-type quartz tube. CO adsorption was considered to be completed after two or three peaks showed the same peak areas, and the difference of first peak area and last peak area was sample adsorption amount. Moreover, a Perkin-Elemer 4500 fluorescence spectrophotometer was used to analyze the photoluminescence (PL) properties of the samples with an excitation wavelength of 310 nm at room temperature.

2.3. Electrochemical measurements. Electrochemical measurements were carried out on an electrochemical station (PARSTAT 2273, Princeton) in a standard three electrode system with the prepared samples as working electrode, a platinum plate as the counter and standard Ag/AgCl electrode as the reference. A 0.02 M

Na_2SO_4 aqueous solution was used as the electrolyte. The photocurrent of the samples was measured under a chopped irradiation from a 350W Xenon lamp (Lap Pu, XQ) with a 420 nm cutoff filter right above the reactor (light on/off cycle: 20 s). The output current for the lamp was controlled to be 15 A with an average intensity of irradiation 97.3 mW/cm^2 determined by a light meter (LI-COR Biosciences, LI-250A). The scan rate for the linear sweep voltammetry (LSV) was 2 mV s^{-1}. The Mott-Schottky plots for the samples were obtained at a frequency of 1.0 KHz, and the electrochemical impedance spectroscopy (EIS) was conducted at a frequency from 0.1 Hz to 100 KHz.

2.4. Photocatalytic performance tests. The photocatalytic CO_2 reduction was conducted in a homemade 250 mL sealed cell with 170 mL of 0.1 M $KHCO_3$ as electrolyte solution.[22] No wire was connected between electrode and sample, and no closed circuit was formed during every photocatalytic CO_2 reduction test. Before reduction, high purity CO_2 (99.99%) gas was passed through the electrolyte solution for 30 min until the CO_2 concentration reached saturation and dissolved oxygen was removed completely. A 350 W Xenon lamp with a 420 nm cutoff filter was used as light source, which was positioned 24 cm away from the reactor to maintain the photocatalytic reaction temperature. The output current for the lamp was controlled to be 8 A with an average intensity of irradiation 1.16 mW/cm^2. All the experiments were performed at room temperature and ambient pressure. The gaseous products evolved during CO_2 photocatalytic reduction were collected by a 1μm syringe and then immediately analyzed by two gas chromatograph instruments. One is GC-2014

(Serial No. C11484403556 SA, SHIMADZU, Japan) equipped with a flame ionization detector (FID) for organic compound detection, the other is GC-2014 (Serial No. C11485013433 SA, SHIMADZU, Japan) with a thermal conductivity detector (TCD) for analysis of inorganic gases. For GC-2014 with FID, a packed column (PROPAK-Q, 2 m × 3 mm) was used, and for GC-2014 with TCD was a different packed column (C36880-14, Restek, 2 m × 1 mm). The carrier gas was nitrogen (N_2). The amount of the evolved products was the average value of three measurements. Control experiments were performed under identical conditions but in the absence of CO_2 (under N_2 atmosphere) or light irradiation. Additionally, the activity of a blank Cu foil and a carbon coated Cu foil (C-Cu) annealed under the same condition were measured in a similar way. For the stability measurements, after each cycle of photoreduction for 3 h, the sample was taken out of the cell and then put into it again for the next cycle reaction under the same reaction conditions. Before each cycle, fresh CO_2 and electrolyte periodically replaced the used ones. The gaseous products collected for isotopic measurement with a gas chromatography-mass spectrometry (Pfeiffer OmniStar) were evolved with the same process mentioned above except that the carbon source of the high purity CO_2 was taken the place of by isotope $^{13}CO_2$ (^{13}C 99%, Sigma-Aldrich).

3. RESULTS AND DISCUSSION

Scheme 1 illustrates the schematic representation of the preparation process of CCMNRs. Briefly, $Cu(OH)_2$ NTs was synthesized through one-step chemical

oxidation of a Cu foil, which was then followed by glucose-coating and thermal reduction to form CCMNRs. The conversion of $Cu(OH)_2$ to Cu_2O was achieved by dehydration of $Cu(OH)_2$ to CuO, followed by oxygen removal from the lattice of CuO to form Cu_2O at high temperature in N_2 atmosphere.[37] Figure S1 (Supporting Information) showed the X-ray diffraction (XRD) pattern of as-prepared $Cu(OH)_2$, which confirmed pure $Cu(OH)_2$ crystal phase without identified Cu_2O and CuO.

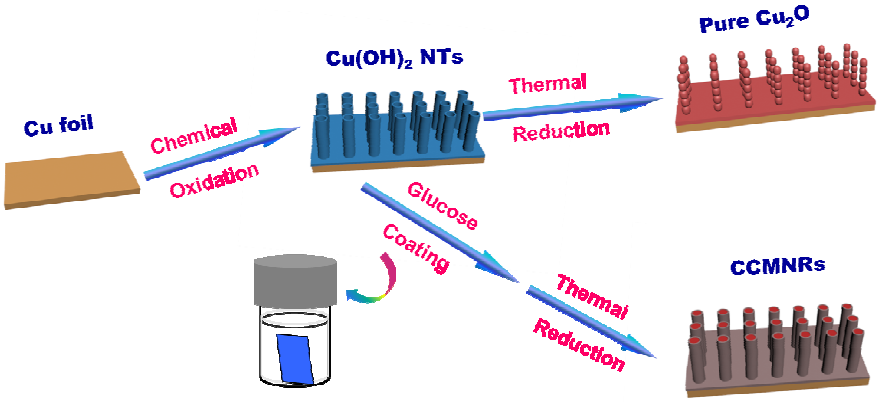

Scheme 1. Schematic illustration of the formation of pure Cu_2O and carbon layer coated Cu_2O mesoporous nanorods (CCMNRs).

A series of carbon coated samples were synthesized with different amount of glucose. Specifically, 1, 2, 3, 4 and 5 mg ml^{-1} of glucose were used, and the samples were denoted with C-x/Cu_2O, in which x represented glucose solution concentration (mg mL^{-1}). Typical XRD patterns recorded from C-2/Cu_2O, along with pure Cu_2O and Cu foil (annealed under the same condition) are shown in Figure 1a. It can be clearly found that besides three peaks for elemental Cu resulted from the Cu substrate, the

others were all assigned to Cu_2O phase with a strong (111) orientation (PDF No.78-2076), and no peaks attributed to CuO or $Cu(OH)_2$ was identified. Figure 1b presents the comparison of the XRD patterns in 15° ~ 29.5° range. Obviously, broad peak around 23° was observed for C-2/Cu_2O, which was ascribed to carbon species.[24]

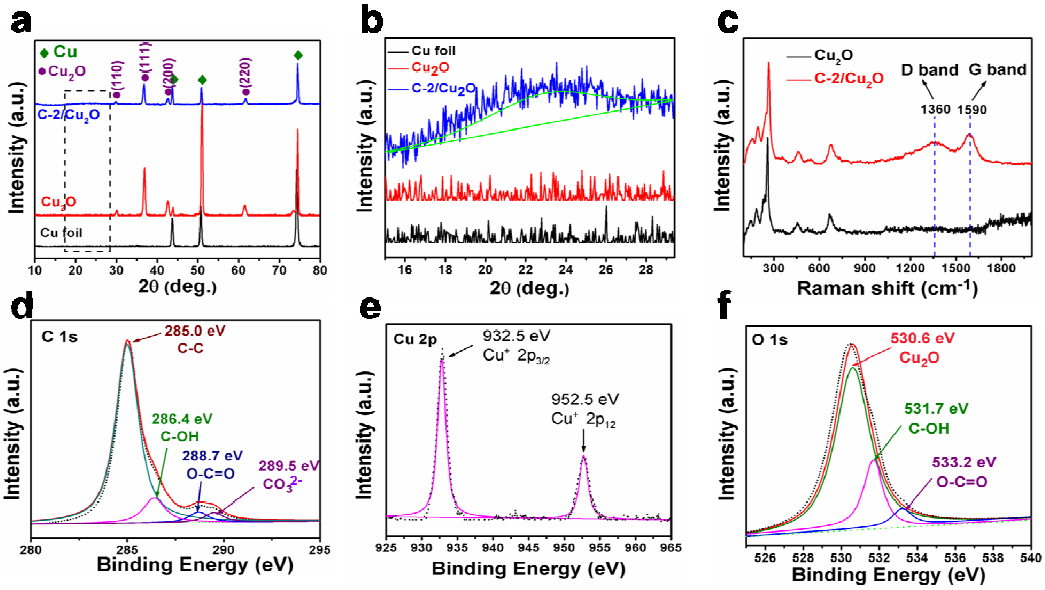

Figure 1. (a) XRD patterns and (b) corresponding enlarged parts in the range of 15° ~ 29.5° (2θ) for Cu foil, pure Cu_2O and C-2/Cu_2O. (c) Raman spectra of pure Cu_2O and C-2/Cu_2O. High resolution XPS spectra of (d) C 1s, (e) Cu 2p, and (f) O 1s for C-2/Cu_2O.

Raman spectra were displayed in Figure 1c to further confirm the presence of carbon in C-2/Cu_2O. Distinct D and G band located at 1360 and 1590 cm^{-1} was present, corresponding to amorphous and graphite carbon respectively,[38] which manifested that carbon was successfully decorated on the surface of C-2/Cu_2O. Additional peaks at 148, 218, 412, and 626 cm^{-1} were assigned to vibrational modes of Cu_2O.[39]

High-resolution XPS spectra for C 1s, Cu 2p, and O 1s are depicted in Figures 1d, 1c and 1f, respectively to verify the elemental composition and chemical state in C-2/Cu_2O. In Figure 1d, the strong C-C peak at 285.0 eV implied the formation of a carbon layer on the Cu_2O surface. The other three peaks with lower intensity at 286.4, 288.7, and 289.5 eV belonged to C-OH, O-C=O, and CO_3^{2-} respectively, which was due to the presence of the adsorbed oxygen functional groups on the carbon layer.[40] From Figure 1e, the sharp and symmetrical peak centered at 932.5 and 952.5 eV was found, corresponding to Cu^+ $2p_{3/2}$ and Cu^+ $2p_{1/2}$ respectively. No evident satellite peak was observed, indicating the absence of Cu^{2+}. From the O 1s core level spectrum in Figure 1f, the same oxygen functional groups adsorbed on the carbon layer were detected. The existence of hydroxyl groups on the surface indicated that H_2O molecules were easily accessible to the surface, which might lead to higher activity for CO_2 photoreduction.[41] The XPS survey spectrum of C-2/Cu_2O is shown in Figure S2 (Supporting Information), from which no evidence was discovered for the formation of a Cu-C bond. So, the above results verified that carbon decorated Cu_2O samples were successfully prepared via the calcination of $Cu(OH)_2$ precursors treated with glucose.

Scanning electron microscopy (SEM) images in Figures 2a~2c reveal the morphology of the prepared samples. Figure 2a showed that the $Cu(OH)_2$ NTs covered almost all surface of copper substrate uniformly and compactly. Pure Cu_2O thin films grown on Cu foil were prepared when the $Cu(OH)_2$ NTs was directly annealed in N_2 atmosphere without glucose-coating. As the SEM images with different magnification

shown in Figure 2b, a nanorod-like morphology composed of aggregated and irregular nanoparticles with a large size of about 200 nm was observed for pure Cu_2O. The fine 1-D nanotube structure disappeared compared with $Cu(OH)_2$ precursor and the composed particle size was large.

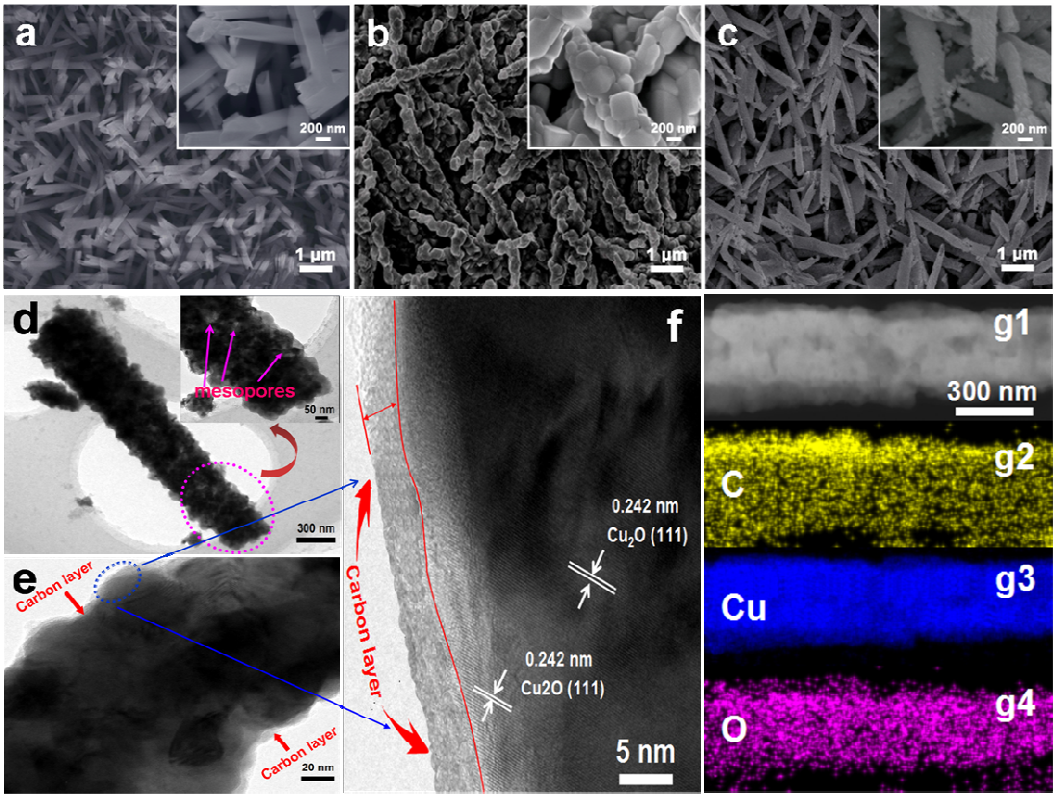

Figure 2. SEM images for (a) $Cu(OH)_2$ NTs, (b) pure Cu_2O, and (c) C-2/Cu_2O (the insets are those with high magnifications). TEM images of C-2/Cu_2O in (d) low magnification (the inset is the detailed image of red dashed part) and (e) high magnification. (f) HRTEM image of C-2/Cu_2O. (g) DF-STEM image of C-2/Cu_2O and corresponding elemental mapping images of C, Cu and O.

When calcined in N_2 after glucose-coating, the $Cu(OH)_2$ NTs were transformed into CCMNRs. The SEM images in Figure 2c displayed that the 1-D structure still

remained for the prepared samples. More importantly, the C-2/Cu_2O sample exhibited a rough but dense surface, which might provide a large specific surface area to trap the incident light efficiently by internal multiscattering.[42] Additionally, the dense carbon coated nanorods could be advantageous for enhanced photostability in electrolyte solution. The SEM images of other C-x/Cu_2O with different glucose concentration are presented in Figure S3 (Supporting Information), from which it can be clearly seen that all the samples possessed 1-D structure as well and the surface of the samples became denser with the increase of glucose concentration. This was attributed to the fact that the thickness of the carbon layer on the surface of CCMNRs increased when increasing glucose concentration, which was validated by the HRTEM images of C-x/Cu_2O with different glucose concentration (Figure S3 in Supporting Information). The different morphology of pure Cu_2O and C-x/Cu_2O indicated that the carbon layer coated on the surface was paramount for the original 1-D morphology retention of $Cu(OH)_2$ NT precursors.

Transmission electron microscopy (TEM) images for C-2/Cu_2O are presented in Figures 2d~2f to explore the nanostructure and amorphous carbon on the surface. As shown in Figure 2d, quintessential nanorod morphology with a length of about 2.2 μm and a width of about 300 nm was distinctly observed. Such a large aspect ratio can be highly in favor of electron diffusion.[43] The insert in Figure 2d was the close observation to the end of a single nanorod, from which mesoporous structure was revealed and a number of mesopores were distributed widely within C-2/Cu_2O. From Figure 2e, it can be seen that the nanorod was composed of nanoparticles with a

diameter of about 20 nm, which was much smaller than that of pure Cu_2O. High-resolution TEM (HRTEM) (Figure 2f) displayed that an amorphous layer with a thickness of about 5 nm was delicately coated on the surface of C-2/Cu_2O, as shown in the marked red line. Typical lattice fringes with an interplanar spacing of 0.242 nm corresponding to the (111) plane for Cu_2O were detected for C-2/Cu_2O, which was in conformity with the XRD result in Figure 1a. Figures 2g1~2g4 showed the dark-field scanning transmission electron microscopy (DF-STEM) and corresponding elemental mapping images of a single nanorod, confirming the presence and uniform distribution of element Cu, O, and C. Figure S4 (Supporting Information) displays a DF-STEM image of another nanorod and corresponding elemental mapping images for C-2/Cu_2O, which further demonstrated that the nanorod was consisted of nanoparticles and there was an uniform coverage of carbon on the surface of Cu_2O nanorods distinctly. Furthermore, pulsed CO chemisorption was performed to measure CO consumption for estimating the coverage extent of carbon layer. Pure Cu_2O sample showed CO chemisorption with an amount of 0.113 cm^3 g^{-1}, consistent with the report that Cu_2O is capable of CO adsorption.[44] However, both C-1/Cu_2O and C-2/Cu_2O showed no CO chemisorption ability, which indicated that the carbon layer totally covered the surface of Cu_2O nanorods, and thus the coverage extent was almost 100%.

To further validate the porous structure of the C-2/Cu_2O sample, N_2 adsorption-desorption isotherms and pore diameter distributions are particularly presented in Figure 3a. A typical mesoporous nature was determined, which was in

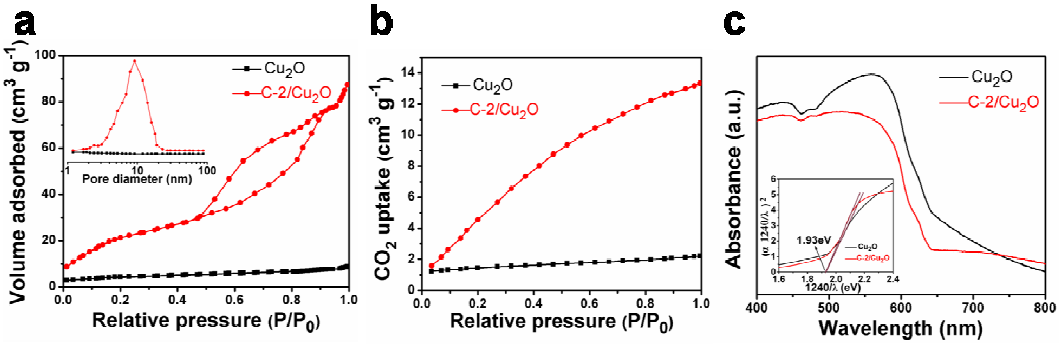

Figure 3. (a) N_2 adsorption-desorption isotherm curves, (b) CO_2 adsorption isotherm curves and (c) UV-vis diffuse reflectance spectra for pure Cu_2O and C-2/Cu_2O. The insert in (a) shows the corresponding pore size distribution, and that in (c) is the plots of $[F(R)]^2$ versus photo energy.

accordance with a type-IV H_2 hysteresis loop curve for C-2/Cu_2O. In contrast, no porous characteristic was observed for pure Cu_2O with surface area around 2.0 m^2 g^{-1}, which was much smaller than C-2/Cu_2O with surface area of 58.93 m^2 g^{-1}. The reason was largely attributed to the carbon layer, which was beneficial to retain the original nanostructure of $Cu(OH)_2$ NTs. In the process of thermal reduction, melted glucose permeated into the voids on the surface of $Cu(OH)_2$ NTs and might be partially pyrolyzed to amorphous carbon.[38] With the presence of carbon layer, C-2/Cu_2O nanorods maintained the mesoporous nanostructure. However, without the protection of carbon, the growth and aggregation of nanograins was not suppressed, leading to the formation of large Cu_2O particles with the deterioration of porous structure. The insert plots were pore size diameter distribution of the samples, and a pore size distribution in the range of 2~20 nm was detected for C-2/Cu_2O, which was in

agreement with the mesopores shown in the TEM image (Figure 2d). Nevertheless, there was no obvious pore size distribution for pure Cu_2O. The large specific surface area and mesoporous structure for C-2/Cu_2O facilitated the adsorption of reactant molecules,[45] which was confirmed by the CO_2 adsorption behavior at room temperature. It is found in Figure 3b that the maximum CO_2 uptake for C-2/Cu_2O was about 13.4 $cm^3 g^{-1}$, which was much higher than that of 2.2 $cm^3 g^{-1}$ for pure Cu_2O.

UV-vis diffuse reflectance spectrum (DRS) presented in Figure 3c was used to probe the optical absorption property and band structure of the materials. The two samples demonstrated excellent visible light absorption in the range of less than 640 nm. Compared with pure Cu_2O, C-2/Cu_2O showed an apparent decreased absorption in visible light region, which implied that the carbon layer prevented the Cu_2O NRs from light harvesting to some extent. This phenomenon was also observed for other C-x/Cu_2O samples as shown in Figure S5 (Supporting Information). Thus, with the increase of carbon thickness, superior conductivity and high strength were achieved whereas light absorption in visible light region was sacrificed. From a combined viewpoint, there existed an optimal carbon thickness, which could bring supreme active performance and stability for CCMNRs as photocatalysts in CO_2 reduction. In this study, the C-2/Cu_2O sample with a thickness of about 5 nm was the optimized one, which would be verified by electrochemical tests below. According to Kubelka-Munk function, the DRS measurements were transformed and plotted against energy of light (insert in Figure 3c),[46] from which the same band gap values of 1.93 eV for pure Cu_2O and C-2/Cu_2O were estimated, indicating that no band gap change was observed

with the carbon layer on the surface of Cu_2O. It further implied that there was no carbon doped into the Cu_2O lattice, which agreed well with the XPS results.

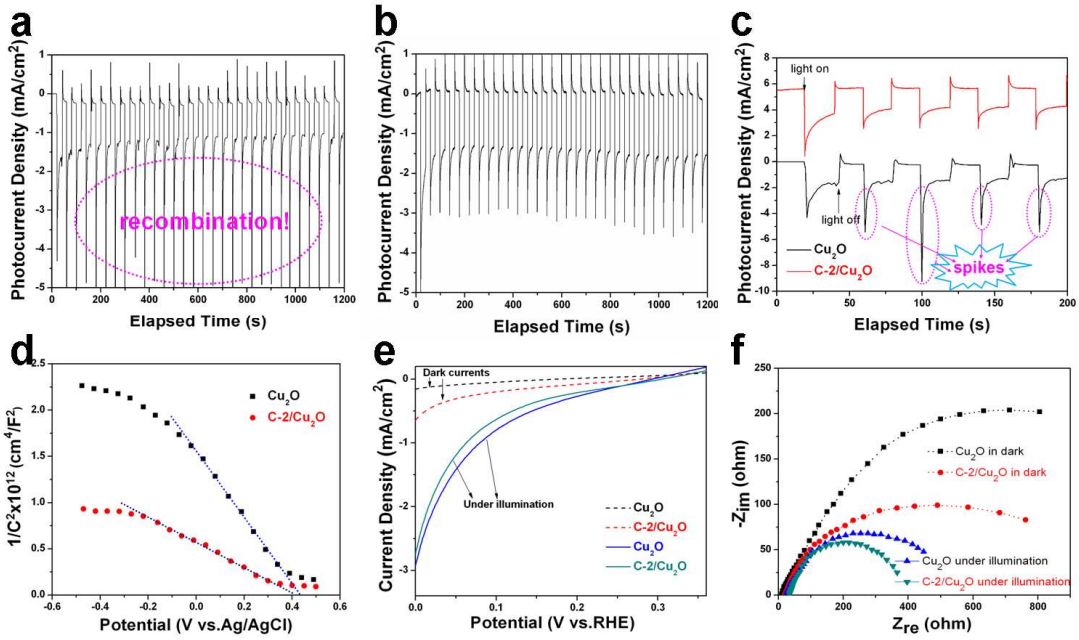

Figure 4. Photocurrent density of (a) pure Cu_2O and (b) C-2/Cu_2O with light on/off cycles under visible light irradiation. (c) Enlarged photocurrent density plots of the first 200 s for pure Cu_2O and C-2/Cu_2O. (d) Mott-Schottky plots of pure Cu_2O and C-2/Cu_2O measured in an aqueous solution of Na_2SO_4 (0.02 M). (e) Linear sweep voltammetry (LSV) curves and (f) electrochemical impedance spectra (EIS) measured in an aqueous solution of Na_2SO_4 (0.02 M) under dark and illumination conditions for pure Cu_2O and C-2/Cu_2O.

Figures 4a and 4b show the photocurrent density for pure Cu_2O and C-2/Cu_2O respectively. It can be found that pure Cu_2O and C-2/Cu_2O owned a photocurrent density of about 2.0 and 2.9 mA cm^{-2} respectively under the first irradiation cycle. The enhanced photocurrent for C-2/Cu_2O was ascribed to the superior conductivity

contributed by the coated carbon layer and efficient charge carrier transfer offered by the 1-D nanostructure. Whereas, the photocurrent decreased rapidly for pure Cu_2O, while only a little decay was observed for C-2/Cu_2O. Here, the photocurrent density at the end of the last light cycle was used to compare with that at the end of the first light cycle within 20 min measurement period for representing the photostability of the samples.[47,48] In comparison with pure Cu_2O with a photostability of only 52%, the photostablility for C-2/Cu_2O increased to be 75%. Indeed, other C-x/Cu_2O samples all exhibited highly improved photostability, as shown in Figure S6 (Supporting Information), and the photostability increased with the increase of glucose concentration during the treatment. Nevertheless, thicker carbon layer hindered the absorption of visible light. So, the photocurrent density dwindled with the increase of glucose concentration for C-x/Cu_2O samples ($x > 1$) (Figure S6 in Supporting Information). Figure S7 (Supporting Information) showed the photocurrent density (at the end of the last light cycle from the photocurrent density plots) and photostability of the C-x/Cu_2O samples as a function of glucose concentration. Considering the two factors, the C-2/Cu_2O sample with a thickness of around 5 nm was regarded as the best one. Figure 4c displays the enlarged photocurrent density plots of the first 200 s to further compare the electrochemical property of pure Cu_2O and C-2/Cu_2O. It can be seen that the instant photocurrent under irradiation was extremely large for pure Cu_2O, but it decreased rapidly on account of the recombination of photogenerated electron-hole pairs, and thus a distinct spike was generated. However, the spikes were small for C-2/Cu_2O, and gradually disappeared with the increase of glucose

concentration for C-x/Cu_2O (Figure S6 in Supporting Information), indicating the low recombination rate of photogenerated electron-hole pairs for the carbon coated samples. Hence, the carbon layer coated on the surface of Cu_2O NRs had a paramount contribution to hinder the recombination of photogenerated electrons and holes, to facilitate the fast electron transfer, as well as to enhance the photostability of Cu_2O.

Mott-Schottky (MS) measurements were performed in order to determine the carrier concentrations and conduction band position of the samples, and the results are shown in Figure 4d. The negative slope indicated that pure Cu_2O and C-2/Cu_2O were p-type semiconductors with hole conduction. The donor concentration of the samples can be quantified by the Mott-Schottky equation [49]

$$1/C^2 = (2/e\varepsilon_0\varepsilon N_A)[(V-V_{FB})-kT/e], \quad (1)$$

where C represents the capacitance of space charge region, e the electron charge, ε_0 the vacuum permittivity, ε the dielectric constant of material (for Cu_2O, $\varepsilon = 6.3$ [50]), V the electrode applied potential, k the Boltzmann constant, T the absolute temperature and N_A the donor concentration. At room temperature, the term of kT/e is calculated to be 25.693 meV, which is exceedingly small and can be neglected. Then the slope determined from the analysis of Mott-Schottky plot can be used to estimate the donor concentration using the following equation [51]

$$N_A = (2/e\varepsilon_0\varepsilon)[d(1/C^2)/dV]^{-1}, \quad (2)$$

So, the hole concentrations were then calculated to be 6.30×10^{18} and 1.69×10^{19} cm^{-3} for pure Cu_2O and C-2/Cu_2O respectively, which was higher than 9.25×10^{17} cm^{-3} for the Cu_2O prepared by electrodeposition method in our previous report.[26]

Additionally, the hole concentration for C-2/Cu_2O was nearly three times as that of pure Cu_2O, which inferred that the carbon layer could accelerate electron transfer and the standard 1-D structure was in favor of charge carrier transfer. In addition, from the MS plots, the flat-band potential (E_{FB}) was also quantified to be 0.436 and 0.414 V (vs.Ag/AgCl) for pure Cu_2O and C-2/Cu_2O respectively. The measured E_{FB} can be converted to the normal hydrogen electrode (NHE) scale via Nernst equation:[18]

$$E_{NHE} = E_{Ag/AgCl} + 0.05916\ \text{pH} + E^0_{Ag/AgCl}, \quad (3)$$

where E_{NHE} is the converted potential vs. NHE, $E_{Ag/AgCl}$ the experimental potential measured against Ag/AgCl reference electrode, and $E^0_{Ag/AgCl}$ the standard potential of Ag/AgCl at 298 K (0.1976 V). Then the conduction-band (E_{CB}) edge was calculated to be -0.734 and -0.756 V for pure Cu_2O and C-2/Cu_2O respectively according to the following equation:

$$E_{FB} - E_{CB} = k_B T \ln(N_V/N_A), \quad (4)$$

where N_A is the carrier density and N_V the effective density of states in the valence band which can be expressed as

$$N_V = 2(2\pi m^* k_B T/h^2)^{3/2}, \quad (5)$$

where $m^* = 0.58m_0$ is taken as the effective hole mass.[39] The calculated conduction-band position was more negative than the reduction potential of CO_2,[52] which might provide a large driving force for CO_2 photoreduction thermodynamically.

Figure 4e displays the linear sweep voltammetry (LSV) curves under dark and illumination conditions for pure Cu_2O and C-2/Cu_2O. The dark current of pure Cu_2O was infinitesimally small due to its poor conductivity, while the dark current became

much large for C-2/Cu_2O with the help of the coating carbon layer. Under illumination, the currents of the two samples increased greatly without doubt. Interestingly, under this condition, the current of pure Cu_2O was just comparable with C-2/Cu_2O, which was due to the reason that the carbon layer blocked the optical absorption. The electrochemical impedance spectra (EIS) shown in Figure 4f were used to analyze the interfacial charge transfer process for the different electrodes in electrolyte. The measurement was conducted in the frequency range of 100 kHz to 0.1 Hz at a potential of 0 V vs Ag/AgCl under dark and illumination conditions. The diameter of the semicircle is indicative of the interfacial charge transfer resistance, R_{ct}, across the electrode/electrolyte interface.[53] Compared with pure Cu_2O, C-2/Cu_2O showed a lower R_{ct} value both in dark and under illumination, which was attributed to the conductivity improvement resulted from the carbon layer on the surface of Cu_2O NRs. The carbon layer facilitated the electron transfer from Cu_2O to the electrolyte, resulting in an overall decrescent charge transfer resistance. The results were also consistent with the LSV and photocurrent results.

Finally, the photocatalytic activity of pure Cu_2O and C-2/Cu_2O toward CO_2 reduction for the formation of hydrocarbon under visible light irradiation was evaluated. In this study, methane (CH_4) and ethylene (C_2H_4) were found to be the major products of CO_2 photoreduction. Control experiments under identical conditions but in the absence of CO_2 (under N_2 atmosphere) or light irradiation were performed, in which no hydrocarbon product was detected. Additionally, the activity of a blank Cu foil and a carbon coated Cu foil (C-Cu) annealed under the same

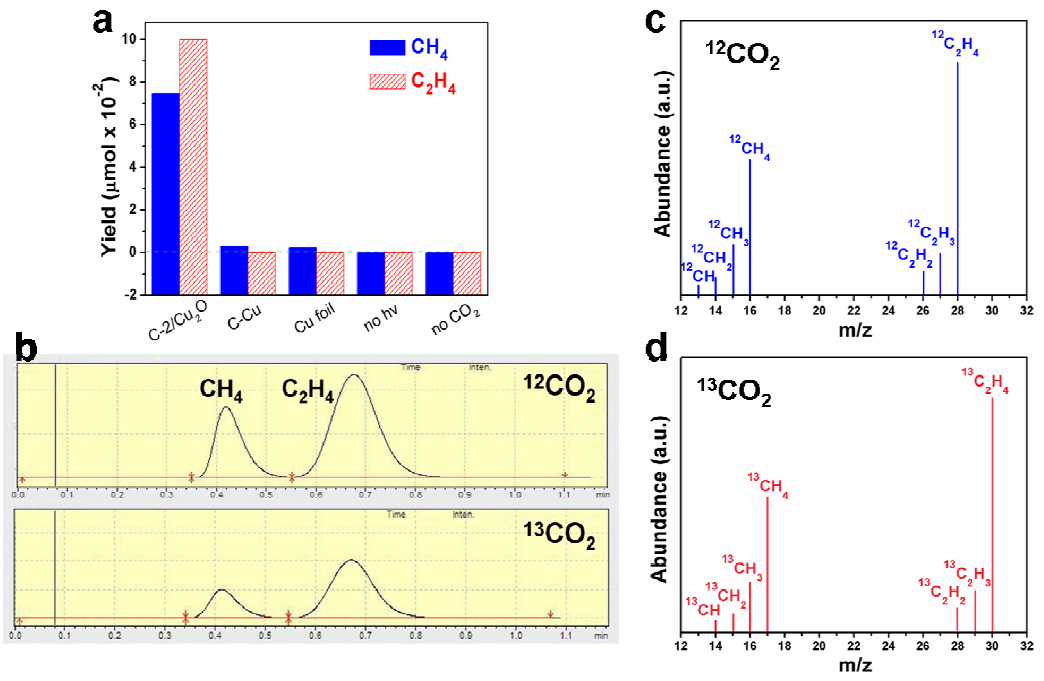

Figure 5. (a) Yield of CH_4 and C_2H_4 evolved from photocatalytic CO_2 reduction for C-2/Cu_2O compared with that of controlled conditions under 6 h irradiation. (b) Gas chromatogram of CH_4 and C_2H_4 evolved from $^{12}CO_2$ and $^{13}CO_2$ as carbon source. Mass spectra after 6 h photocatalytic reduction of (c) $^{12}CO_2$ and (d) $^{13}CO_2$.

condition were measured for comparison as well. The results for 6 h photocatalytic reaction are displayed in Figure 5a. It can be seen that the annealed Cu foil and carbon coated Cu foil just had negligible activity toward CO_2 photoreduction but the sample C-2/Cu_2O produced a large amount of hydrocarbon. ^{13}C-labeled isotopic experiment was also carried out to provide solid evidence for validating the origin of the evolved products, in which $^{13}CO_2$ was used to replace $^{12}CO_2$. In Figure 5b, two peaks at retention time of 0.42 and 0.68 min were assigned to CH_4 and C_2H_4 respectively. Figure 5c and 5d showed the mass spectrum after 6 h photocatalytic conversion of

$^{12}CO_2$ and $^{13}CO_2$ respectively. When $^{13}CO_2$ was the reactant, $^{13}CH_4$ (m/z = 17) and $^{13}C_2H_4$ (m/z = 30) were detected, which was significantly different from the signal for $^{12}CH_4$ (m/z = 16) and $^{16}C_2H_4$ (m/z = 28) when using $^{12}CO_2$ as the reactant. This is the direct evidence to prove that the carbon source for the evolved hydrocarbons came from CO_2 but not from carbon layer or any other carbon source.

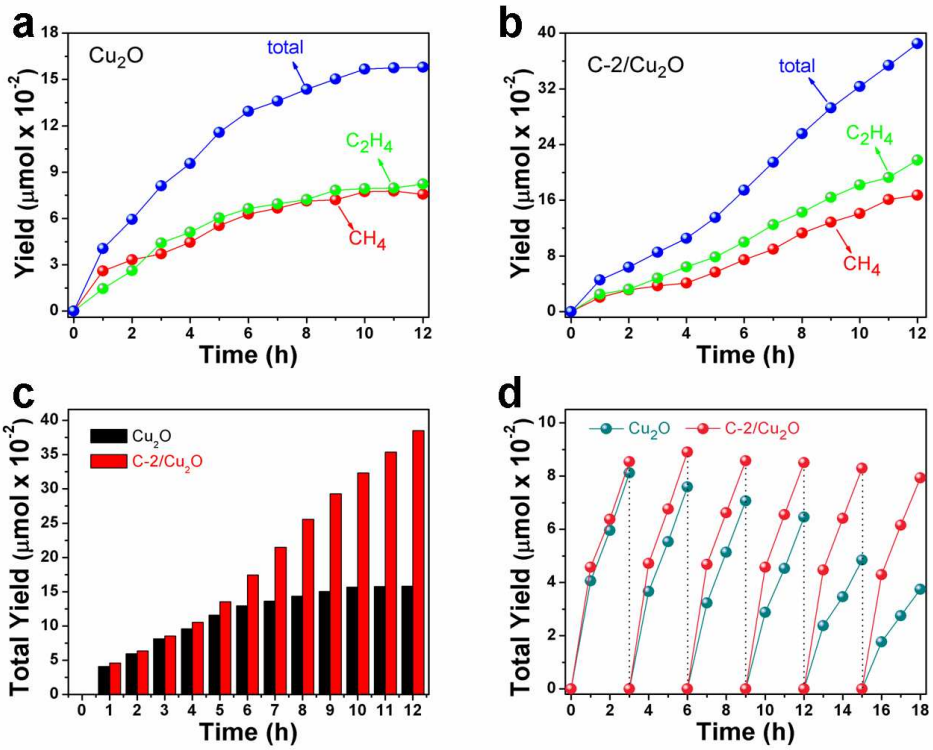

Figure 6. Time-dependent product evolution over (a) pure Cu_2O and (b) C-2/Cu_2O. (c) Histogram of total yield and (d) stability study of photocatalytic evolution (CH_4 and C_2H_4) for pure Cu_2O and C-2/Cu_2O under visible light irradiation.

The yield of CH_4 and C_2H_4 on the prepared photocatalysts as a function of irradiation time was plotted in Figures 6a and 6b. As shown in Figure 6a, for pure Cu_2O sample, the total yield of CH_4 and C_2H_4 increased rapidly within 5 h, but

thereafter the conversion rates diminished gradually for another 4 h, and finally the concentration of the formed organic compounds remained unchanged in the last few hours. This was presumably due to the ubiquitous issue of photocorrosion for Cu_2O. Substantially, the total yield of CH_4 and C_2H_4 increased gradually within the whole irradiation time for C-2/Cu_2O sample (Figure 6b). The total amount of CH_4 and C_2H_4 reached 0.385 μmol after 12 h visible light irradiation, which was 2.5 times as high as that for pure Cu_2O. The histogram of the total yield of CH_4 and C_2H_4 in Figure 6c displayed a further comparison for pure Cu_2O and C-2/Cu_2O. The total yield of pure Cu_2O was barely comparable to that of C-2/Cu_2O in the preliminary 4 h, but it then fell behind with further irradiation. We checked the durability of C-2/Cu_2O for CO_2 reduction carefully. Figure S8a (Supporting Information) showed the total yield (CH_4 and C_2H_4) evolution over C-2/Cu_2O during prolonged irradiation up to 34 h. It can be found that the photocatalyst still maintained most of its intrinsic photocatalytic activity after 28 h, indicating that the durability of C-2/Cu_2O was much better than that of pure Cu_2O. Additionally, the apparent quantum efficiency (AQE) of CH_4 and C_2H_4 was calculated to be 0.71% and 1.36% respectively, and the total AQE was thus 2.07% for C-2/Cu_2O at λ_0 = 400 nm. The details for the calculation process are shown in Supporting Information. The AQE of 2.07% was higher than that for the published Cu_2O-based photocatalysts such as Cu_2O/reduced graphene oxide composites (AQE = 0.34%)[54] and Cu_2O/RuO_x composites (AQE = 1.6%)[55]. A detailed comparison with the AQE values for other representative photocatalysts is presented in Table S1 in Supporting Information, which showed the AQE of 2.07% was decent. Most

importantly, neither catalyst hybridization nor cocatalyst was used in our engineered material. Another effective strategy like photoelectrocatalysis (PEC) combining the merits of both electrocatalysis (EC) and photocatalysis (PC) in our future work is anticipated to further improve the CO_2 conversion efficiency over C-2/Cu_2O. The results of other C-x/Cu_2O toward CO_2 photoreduction under the same condition were shown in Figure S8b (Supporting Information).

To further testify the recycling photostability of as-prepared photocatalysts, repeated CO_2 photoreduction experiments were conducted for six cycles with every cycle of 3 h under the same reaction conditions. The data are shown in Figure 6d. It can be seen that significant deactivation was observed along with prolonged reaction duration for pure Cu_2O. The total yield of CH_4 and C_2H_4 decreased to 0.037μmol in the sixth cycle, merely about 46% of that for the first run. While the photocatalytic activity of C-2/Cu_2O almost remained after six cycles with total yield of CH_4 and C_2H_4 0.079 μmol in the sixth cycle, just about 7% loss compared to that for the first run. So, C-2/Cu_2O had superior stability to pure Cu_2O for CO_2 photoreduction.

In order to probe the specific structure change for pure Cu_2O and C-2/Cu_2O during the CO_2 reduction under irradiation, SEM images of the samples after three and six reaction cycles were collected and presented in Figures 7a1 and 7b1, and Figures 7a2 and 7b2, respectively. For pure Cu_2O, the large particles were aggregated to some lumps after three cycles, then totally agglomerated and fused after six cycles. However, the 1-D nanorod architecture remained for C-2/Cu_2O, and the size for the nanorods became just slightly larger after six cycles, validating the high stability of

the nanostructure for CCMNRs.

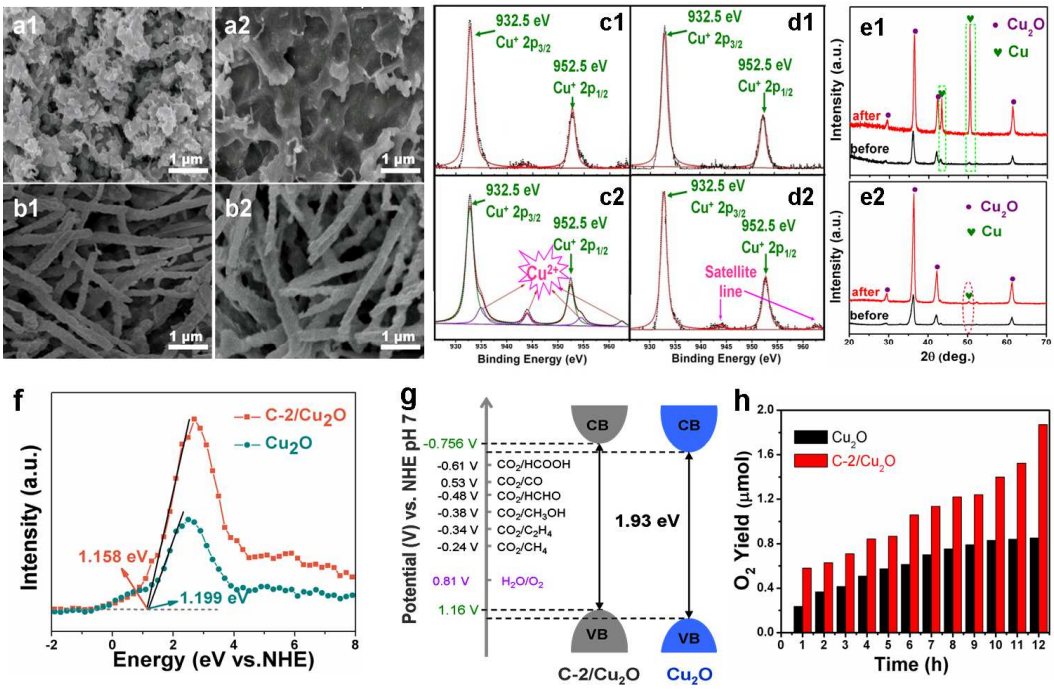

Figure 7. SEM images of pure Cu_2O (a1 and a2), and C-2/Cu_2O (b1 and b2) after three (a1 and b1) and six (a2 and b2) reaction cycles of CO_2 reduction. High resolution XPS spectra of Cu 2p for pure Cu_2O (c1 and c2), and C-2/Cu_2O (d1 and d2) before (c1 and d1) and after (c2 and d2) six cycles of CO_2 reduction. Surface XRD patterns of pure Cu_2O (e1) and C-2/Cu_2O (e2) before and after six cycles of CO_2 reduction under visible light irradiation. (f) XPS valence-band spectra, and (g) band structure alignments of pure Cu_2O and C-2/Cu_2O. (h) Time courses of photocatalytic O_2 production over pure Cu_2O and C-2/Cu_2O under visible light irradiation.

XPS detections were also performed to analyze the composition change of the two samples after six reaction cycles. The Cu 2p core level spectra are shown in Figures 7c1, 7c2, 7d1 and 7d2, from which it can be seen that for pure Cu_2O, a new peak at

935.6 eV emerged and the satellite peaks became stronger, indicating the presence of CuO [56] after six cycles (Figure 7c2). While the Cu 2p spectrum for C-2/Cu_2O had almost no change with only the presence of tiny satellite peaks (Figure 7d2). The formation of Cu^{2+} after photoreduction was mainly originated from the photocorrosion process, in which Cu^+ was oxidized by holes.[57] Yet, Cu^+ and Cu^0 are indistinguishable from the XPS spectrum resulted from the binding energy overlap of Cu^+ and Cu^0 in Cu 2p3/2 region.[58] So, it is necessary to use other technique such as surface X-ray diffraction (SXRD) with corrected background. As shown in Figure 7e2, all peaks in the SXRD pattern of C-2/Cu_2O after CO_2 photoreduction well matched to those for the fresh sample before reaction except a new tiny peak (50.4°), which belonged to Cu^0. Whereas, for pure Cu_2O, two evident diffraction peaks of Cu^0 with a strong intensity were present (Figure 7e1), indicating that most Cu_2O was reduced to Cu^0 after photoreduction reaction. Unfortunately, Cu has no photocatalytic activity. No diffraction peak corresponding to CuO was observed from the SXRD pattern, which was presumably due to its tiny amount on the surface. All the above confirmed the high stability of CCMNRs, which definitely accounted for the maintained performance of CO_2 photoreduction in prolonged duration.

The mechanism of CO_2 photoreduction is complex, and multielectron transfer process is generally considered.[59] The evolved products closely depend on the number of electrons involved in the reduction as well as the reduction potential of different products, as shown in Equations (6) ~ (11) [52]

$$CO_2 + 2H^+ + 2e^- \rightarrow HCOOH,\ E_0 = -0.61\ V\ vs.\ NHE\ at\ pH\ 7 \quad (6)$$

$CO_2 + 2H^+ + 2e^- \rightarrow CO + H_2O$, E_0 = -0.53 V vs. NHE at pH 7 (7)

$CO_2 + 4H^+ + 4e^- \rightarrow HCHO + H_2O$, E_0 = -0.48 V vs. NHE at pH 7 (8)

$CO_2 + 6H^+ + 6e^- \rightarrow CH_3OH + H_2O$, E_0 = -0.38 V vs. NHE at pH 7 (9)

$CO_2 + 8H^+ + 8e^- \rightarrow CH_4 + 2H_2O$, E_0 = -0.24 V vs. NHE at pH 7 (10)

$2CO_2 + 8H_2O + 12e^- \rightarrow C_2H_4 + 12OH^-$, E_0 = -0.34 V vs. NHE at pH 7 (11)

The conduction-band position of pure Cu_2O and C-2/Cu_2O calculated from the MS plots was more negative than all the reduction potential of the above mentioned products. Besides, the more negative reduction potential than that for HCOOH, CO, HCHO and CH_3OH formation, the more feasible formation of CH_4 and C_2H_4 thermodynamically.[60] Additionally, a multitude of electrons were supplied for the formation of CH_4 and C_2H_4 in this system since the carbon layer facilitated photogenerated electron transfer to the surface, which facilitated the formation of CH_4 and C_2H_4.[17] So in this study, CH_4 and C_2H_4 were the major products. Withal, the formation products may be also relevant to the morphology of the samples, which affects CO_2 adsorption on the surface.[22] Our previous study revealed a similar phenomenon with electrodeposited Cu_2O thin films on Cu foil as photocatalysts.[22]

It is emphasized that the photogenerated holes can also play a vital role in CO_2 photoreduction along with the photogenerated electrons, since the holes may react with water to evolve oxygen or otherwise recombine with electrons.[17] XPS valence-band spectra were analyzed to investigate the band edges of pure Cu_2O and C-2/Cu_2O. As shown in Figure 7f, the valence-band position was determined to be 1.199 and 1.158 V vs NHE for pure Cu_2O and C-2/Cu_2O respectively, nearly in

agreement with the calculated results from the MS plots. The band structure alignments of pure Cu_2O and C-2/Cu_2O are schematically demonstrated in Figure 7g, which showed that the valence-band (E_{VB}) edges of pure Cu_2O and C-2/Cu_2O were located below the oxidation potential of water ($E^{\theta}(H_2O/O_2)$ = 0.81 V at pH = 7 [61]). Therefore, the formation of oxygen is a thermodynamically favored process here. Substantially, O_2 was indeed detectable for both pure Cu_2O and C-2/Cu_2O in this study. Figure S9 (Supporting Information) showed gas chromatograms of O_2 evolved from the photoreduction of C-2/Cu_2O under different irradiation time. It can be found in Figure 7h that for C-2/Cu_2O, the evolved O_2 amount was much more than that for pure Cu_2O, which was consistent with the results of CH_4 and C_2H_4 evolution shown in Figure 6c. As elucidated above, for pure Cu_2O, considerable quantity of holes reacted with Cu_2O to form CuO and recombined with electrons stemming from the low separation efficiency of electron-hole pairs. While with the help of the coating carbon layer for C-2/Cu_2O, the fast electron transfer rendered a substantial part of holes for the reaction with H_2O to generate O_2, so the evolved O_2 amount was more than that for pure Cu_2O, especially in the prolonged duration.

Since the annealed Cu foil and carbon coated Cu foil just showed negligible activity toward CO_2 photoreduction, the catalytic effect of carbon layer can be ruled out. Based on the photocatalytic reaction results, it is believed that something contributed by the coated carbon layer may play a vital role for the favorable active performance and superior stability for CO_2 photoreduction. It is well known that the 1-D structure, porous structure, big surface area, high separation efficiency of

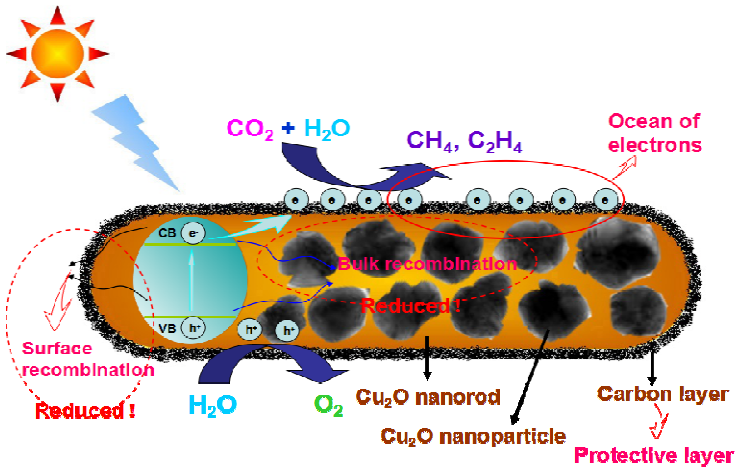

Scheme 2. Schematic diagram of proposed process of CO_2 reduction over CCMNRs under visible light irradiation.

electron-hole pairs and fast electron transfer are overwhelmingly significant for a pleasurable performance of a photocatalyst.[62] In this study, the C-2/Cu_2O sample possessed a quintessential mesoporous 1-D nanorod structure composed of nanoparticles, which was not only in favor of charge carrier transfer but also trapping incident light efficiently. The mesoporous structure owning a large surface area gave rise to the exposure of more active sites, the effective movement of CO_2 molecule,[24] and preferable CO_2 adsorption ability. On the other hand, the carbon layer coated on the Cu_2O nanorods contributed greatly to CO_2 photoreduction. Firstly, the carbon layer worked as a protective layer to quench the photocorrosion of Cu_2O, improving the stability and resistance toward reduction to Cu^0 or oxidation to CuO, which was validated by the XPS and SXRD experiments before and after six cycles. Secondly, a large number of electrons and holes were generated by Cu_2O under visible light irradiation. Owing to the superior conductivity, the electrons moved to the carbon

layer rapidly, thus improving the separation efficiency of electron-hole pairs and suppressing their recombination. The high carrier concentrations calculated from the MS plots, the promoted and stable photocurrent, the low interfacial charge transfer resistance and the weak intensity of emission peak from the photoluminescence (PL) spectra shown in Figure S10 (Supporting Information) were all convincing evidences authenticating the function of the carbon layer. Consequently, a multitude of electrons transferred to the carbon layer, making it an ocean of electrons. Such plentiful electrons were beneficial for CO_2 photoreduction. Based on the above discussion, a schematic diagram of the proposed process of CO_2 reduction over CCMNRs is displayed in Scheme 2.

CONCLUSIONS

Carbon layer coated cuprous oxide (Cu_2O) mesoporous nanorods have been successfully synthesized via a handy method of chemical oxidation and subsequent carbonization. This straightforward “hitting three birds with one stone” strategy endows the samples with three characteristics: coating protective carbon layer, mesoporous structures and 1-D nanostructures of nanorods. Outstanding electrical conductivity rendered by the carbon layer coated on the surface of Cu_2O nanorods, in combination with the 1-D nanostructure, gives rise to the significant improvement of electron transfer, thus suppressing the recombination of electron-hole pairs. Simultaneously, the mesoporous structure provides a large surface area with a host of active sites for the improved CO_2 adsorption. In addition, the carbon layer also

functions as a protective layer to improve the photostability of Cu_2O. Benefiting from the above advantages, the CCMNRs not only possess excellent photocatalytic CO_2 reduction performance with AQE of 2.07% for CH_4 and C_2H_4 at λ_0 = 400 nm, but also exhibit outstanding stability with 93% activity retention after six cycles under visible light irradiation. Above all, this work not only engineers Cu_2O into an efficient and stable photocatalyst but also presents a simple and affordable approach to design protective layer coated architectures for CO_2 conversion under renewable energy.

ASSOCIATED CONTENT

Supporting Information

XRD of $Cu(OH)_2$ NTs, XPS survey spectrum of C-2/Cu_2O, SEM and HRTEM images of C-x/Cu_2O (x = 1, 3, 4, 5), DF-STEM image of another C-2/Cu_2O nanorod and corresponding elemental mapping images, UV-vis DRS spectra of pure Cu_2O and C-x/Cu_2O, photocurrent density plots of C-x/Cu_2O (x = 1, 3, 4, 5), the relationship of glucose concentration and the carbon layer thickness of C-x/Cu_2O, photocurrent density and photostability of C-x/Cu_2O as a function of glucose concentration, total yield (CH_4 and C_2H_4) over C-2/Cu_2O with prolonged irradiation, time-dependent product evolution over C-x/Cu_2O, gas chromatograms of O_2, PL spectra of pure Cu_2O and C-2/Cu_2O, photocatalytic activity of C-2/Cu_2O for AQE determination, AQE comparison, AQE calculations and reaction pathway analysis for the electrons and holes generated from pure Cu_2O and C-2/Cu_2O.

AUTHOR INFORMATION

Corresponding Author

* Email: yuying01@mail.ccnu.edu.cn, tel: 86-27-67867037.

Notes

The authors declare no competing financial interest.

ACKNOWLEDGEMENTS

We would like to thank Prof. Jiaguo Yu from Wuhan University of Technology for CO chemisorption detection. This work was financially supported by National Science Foundation of China (Nos. 21377044 and 21573085), the Key Project of Natural Science Foundation of Hubei Province (No. 2015CFA037), and excellent doctorial dissertation cultivation grant from Central China Normal University (No. 2015YBYB103).

REFERENCES

(1) Yu, J.; Low, J.; Xiao, W.; Zhou, P.; Jaroniec, M. *J. Am. Chem. Soc.* **2014**, 136, 8839-8842.

(2) Tu, W.; Zhou, Y.; Zou, Z. *Adv. Mater.* **2014**, 26, 4607-4626.

(3) Jin, J.; Yu, J.; Guo, D.; Cui, C.; Ho, W. *Small* **2015**, 11, 5262-5271.

(4) Shown, I.; Hsu, H.-C.; Chang, Y.-C.; Lin, C.-H.; Roy, P. K.; Ganguly, A.; Wang, C.-H.; Chang, J.-K.; Wu, C.-I.; Chen, L.-C. *Nano Lett.* **2014**, 14, 6097-6103.

(5) Inoue, T.; Fujishima, A.; Konishi, S.; Honda, K. *Nature* **1979**, 277, 637-638.

(6) Gordon, T. R.; Cargnello, M.; Paik, T.; Mangolini, F.; Weber, R. T.; Fornasiero, P.; Murray, C. B. *J. Am. Chem. Soc.* **2012**, 134, 6751-6761.

(7) Gombac, V.; Sordelli, L.; Montini, T.; Delgado, J. J.; Adamski, A.; Adami, G.; Cargnello, M.; Bernal, S.; Fornasiero, P. *J. Phys. Chem. A* **2010**, 114, 3916-3925.

(8) Li, Y.-F.; Xu, D.; Oh, J. I.; Shen, W.; Li, X.; Yu, Y. *ACS Catal.* **2012**, 2, 391-398.

(9) Takeda, H.; Koizumi, H.; Okamoto, K.; Ishitani, O. *Chem. Commun.* **2014**, 50, 1491-1493.

(10) Sato, S.; Morikawa, T.; Kajino, T.; Ishitani, O. *Angew. Chem. Int. Ed*. **2013**, 125, 1022-1026.

(11) Frogneux, X.; Blondiaux, E.; Thuery, P.; Cantat, T. *ACS Catal.* **2015**, 5, 3983-3987.

(12) Chen, Y.; Kanan, M. W. *J. Am. Chem. Soc.* **2012**, 134, 1986-1989.

(13) Galvez, M.; Loutzenhiser, P.; Hischier, I.; Steinfeld, A. *Energy Fuels* **2008**, 22, 3544-3550.

(14) Wang, Y.; Wang, F.; Chen, Y.; Zhang, D.; Li, B.; Kang, S.; Li, X.; Cui, L. *Appl. Catal. B: Environ.* **2014**, 147, 602-609.

(15) Navalón, S.; Dhakshinamoorthy, A.; Álvaro, M.; Garcia, H. *ChemSusChem* **2013**, 6, 562-577.

(16) Wang, K.; Li, Q.; Liu, B.; Cheng, B.; Ho, W.; Yu, J. *Appl. Catal. B: Environ.* **2015**, 176, 44-52.

(17) Wang, J.-C.; Zhang, L.; Fang, W.-X.; Ren, J.; Li, Y.-Y.; Yao, H.-C.; Wang, J.-S.; Li, Z.-J. *ACS Appl. Mater. Interfaces* **2015**, 7, 8631-8639.

(18) Li, M.; Zhang, L.; Fan, X.; Zhou, Y.; Wu, M.; Shi, J. *J. Mater. Chem. A* **2015**, 3, 5189-5196.

(19) Li, Y.-F.; Zhang, W.-P.; Shen, X.; Peng, P.-F.; Xiong, L.-B.; Yu, Y. *Chin. J. Catal.* **2015**, 36, 2229-2236.

(20) Shi, H.; Chen, G.; Zhang, C.; Zou, Z. *ACS Catal.* **2014**, 4, 3637-3643.

(21) Barreca, D.; Fornasiero, P.; Gasparotto, A.; Gombac, V.; Maccato, C.; Montini, T.; Tondello, E. *ChemSusChem* **2009**, 2, 230-233.

(22) Ba, X.; Yan, L.-L.; Huang, S.; Yu, J.; Xia, X.-J.; Yu, Y. *J. Phys. Chem. C* **2014**, 118, 24467-24478.

(23) Montini, T.; Gombac, V.; Sordelli, L.; Delgado, J. J.; Chen, X.; Adami, G.; Fornasiero, P. *ChemCatChem* **2011**, 3, 574-577.

(24) Wu, R.; Zhang, J.; Shi, Y.; Liu, D.; Zhang, B. *J. Am. Chem. Soc.* **2015**, 137, 6983-6986.

(25) Gerischer, H. *J. Electroanal. Chem*. **1977**, 82, 133-143.

(26) Yu, L.; Xiong, L.; Yu, Y. *J. Phys. Chem. C* **2015**, 119, 22803-22811.

(27) McShane, C. M.; Choi, K.-S. *J. Am. Chem. Soc.* **2009**, 131, 2561-2569.

(28) Siegfried, M. J.; Choi, K.-S. *J. Am. Chem. Soc.* **2006**, 128, 10356-10357.

(29) Xu, H.; Ouyang, S.; Liu, L.; Wang, D.; Kako, T.; Ye, J. *Nanotechnology* **2014**, 25, 165402.

(30) Tan, Y.; Xue, X.; Peng, Q.; Zhao, H.; Wang, T.; Li, Y. *Nano Lett*. **2007**, 7, 3723-3728.

(31) Zhang, Z.; Zhang, L.; Hedhili, M. N.; Zhang, H.; Wang, P. *Nano Lett.* **2012**, 13, 14-20.

(32) Lin, C.-Y.; Lai, Y.-H.; Mersch, D.; Reisner, E. *Chem. Sci.* **2012**, 3, 3482-3487.

(33) Low, J.; Cheng, B.; Yu, J.; Jaroniec, M. *Energy Storage Mater.* **2016**, 3, 24-35.

(34) Feng, Y.; Zhang, H.; Zhang, Y.; Li, X.; Wang, Y. *ACS Appl. Mater. Interfaces* **2015**, 7, 9203-9210.

(35) Hu, Y.; Gao, X.; Yu, L.; Wang, Y.; Ning, J.; Xu, S.; Lou, X. W. D. *Angew. Chem.* **2013**, 125, 5746-5749.

(36) Zhang, W.; Wen, X.; Yang, S.; Berta, Y.; Wang, Z. L. *Adv. Mater.* **2003**, 15, 822-825.

(37) Lu, C.; Qi, L.; Yang, J.; Zhang, D.; Wu, N.; Ma, J. *J. Phys. Chem. B* **2004**, 108, 17825-17831.

(38) Gao, L.; Liu, R.; Hu, H.; Li, G.; Yu, Y. *Nanotechnology* **2014**, 25, 175402.

(39) Li, C.; Li, Y.; Delaunay, J.-J. *ACS Appl. Mater. Interfaces* **2013**, 6, 480-486.

(40) Tang, L.; Ji, R.; Cao, X.; Lin, J.; Jiang, H.; Li, X.; Teng, K. S.; Luk, C. M.; Zeng, S.; Hao, J. *ACS Nano* **2012**, 6, 5102-5110.

(41) Ikeue, K.; Yamashita, H.; Anpo, M.; Takewaki, T. *J. Phys. Chem. B* **2001**, 105, 8350-8355.

(42) Zhou, H.; Guo, J.; Li, P.; Fan, T.; Zhang, D.; Ye, J. *Sci. Rep.* **2013**, 3, 1667-1676.

(43) Archana, P.; Jose, R.; Vijila, C.; Ramakrishna, S. *J. Phys. Chem. C* **2009**, 113, 21538-21542.

(44) Sun, B. Z.; Chen, W. K.; Xu, Y. J. *J. Chem. Phys.* **2009**, 131, 174503.

(45) Zhou, W.; Li, W.; Wang, J.-Q.; Qu, Y.; Yang, Y.; Xie, Y.; Zhang, K.; Wang, L.; Fu, H.; Zhao, D. *J. Am. Chem. Soc.* **2014**, 136, 9280-9283.

(46) Yang, F.; Yan, N.-N.; Huang, S.; Sun, Q.; Zhang, L.-Z.; Yu, Y. *J. Phys. Chem. C* **2012**, 116, 9078-9084.

(47) Paracchino, A.; Brauer, J. C.; Moser, J.-E.; Thimsen, E.; Graetzel, M. *J. Phys. Chem. C* **2012**, 116, 7341-7350.

(48) Paracchino, A.; Mathews, N.; Hisatomi, T.; Stefik, M.; Tilley, S. D.; Grätzel, M. *Energy Environ. Sci.***2012**, 5, 8673-8681.

(49) Jiang, T.; Xie, T.; Chen, L.; Fu, Z.; Wang, D. *Nanoscale* **2013**, 5, 2938-2944.

(50) Wang, L.; Tao, M. *Solid-State Lett.* **2007**, 10, H248-H250.

(51) Yang, X.; Wolcott, A.; Wang, G.; Sobo, A.; Fitzmorris, R. C.; Qian, F.; Zhang, J. Z.; Li, Y. *Nano Lett.* **2009**, 9, 2331-2336.

(52) Li, X.; Wen, J.; Low, J.; Fang, Y.; Yu, J. *Sci. China Mater.* **2014**, 57, 70-100.

(53) Hong, S. J.; Lee, S.; Jang, J. S.; Lee, J. S. *Energy Environ. Sci.* **2011**, 4, 1781-1787.

(54) An, X.; Li, K.; Tang, J. *ChemSusChem* **2014**, 7, 1086-1093.

(55) Pastor, E.; Pesci, F. M.; Reynal, A.; Handoko, A. D.; Guo, M.; An, X.; Cowan, A. J.; Klug, D. R.; Durrant, J. R.; Tang, J. *Phys. Chem. Chem. Phys.* **2014**, 16, 5922-5926.

(56) Balamurugan, B.; Mehta, B.; Shivaprasad, S. *Appl. Phys. Lett.* **2001**, 79, 3176.

(57) Bessekhouad, Y.; Robert, D.; Weber, J.-V. *Catal. Today* **2005**, 101, 315-321.

(58) McShane, C. M.; Choi, K.-S. *Phys. Chem. Chem. Phys.* **2012**, 14, 6112-6118.

(59) Morris, A. J.; Meyer, G. J.; Fujita, E. *Acc. Chem. Res.* **2009**, 42, 1983-1994.

(60) Wang, W.-N.; An, W.-J.; Ramalingam, B.; Mukherjee, S.; Niedzwiedzki, D. M.; Gangopadhyay, S.; Biswas, P. *J. Am. Chem. Soc.* **2012**, 134, 11276-11281.

(61) Kudo, A.; Miseki, Y. *Chem. Soc. Rev.* **2009**, 38, 253-278.

(62) Low, J.; Yu, J.; Ho, W. *J. Phys. Chem. Lett.* **2015**, 6, 4244-4251.

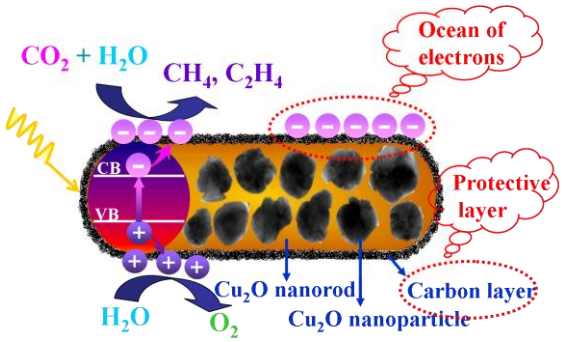

For Table of Contents Only